DOI: 10.13009/EUCASS2017-32

DOI: ADD DOINUMBER HERE

Numerical Model of an Helicon Plasma Source for Space Propulsion Application

M. Magarotto[⋆†]*, F.J. Bosi*[⋆]*, P. de Carlo*[⋆]*, G. Gallina*[⋆]*, M. Manente*[⋆]*, F. Trezzolani*[⋆]*, D. Pavarin*[⋆] *and D. Melazzi*[⋆]
[⋆]*University of Padova, CISAS G.Colombo*
Via Venezia 15, 35131 Padova, Italy
mirko.magarotto@studenti.unipd.it
[†]Corresponding author

Abstract

We have developed a numerical tool devoted to the design and the optimization of an Helicon plasma source employed in an Helicon Plasma Thruster. Our tool is specifically conceived to model high density (higher than $> 10^{18}$ m^{-3}) Helicon plasma sources. The tool is realized coupling ADAMANT, an Electro Magnetic solver which solves for the wave propagation and in turn the power deposition, and OpenFOAM, an open-source C++ library in which we have implemented the fluid transport model. We have developed three versions of the tool, namely 1D-axial, 1D-radial, and 2D-radial-axial. First we have benchmarked our tool against a well-established solver; than we have compared the results given by the three versions of the tool among each other and against a 0D global model for a fixed source configuration. The three models grasp the main features of the Helicon sources and show a better agreement among themselves and with the 0D model in absence of magnetic field.

1. Introduction

In the last two decades several new plasma based propulsion concepts have been proposed and developed, and now are beginning to challenge the monopole of chemical thrusters in space propulsion. Plasma based propulsion systems have a series of advantages in respect to chemical rockets: i) high specific impulse which allows for a huge reduction of propellant mass, and in turn of costs, ii) high thrust efficiency. Plasma propulsion systems are characterized by a low thrust, therefore they have been employed in interplanetary missions[1] and in the position and attitude control systems of missions with high demanding requirements.[2] At the state of the art the most widely employed plasma thrusters are Ion Engines (IE), and Hall Effect Thrusters (HET). Both these concepts are characterized by high efficiency but present some critical issues: i) lifetimes are limited by the erosion of the extracting grids and the ceramic walls; ii) external cathodes are necessary for charge compensation.

Recent advances in plasma-based propulsion systems have led to the development of Helicon Plasma Thrusters (HPTs) (see Figure 1), whose plasma generation system is derived from high-density industrial plasma sources.[3] The principal elements of an HPT are a gas feeding system which provides the neutral gas to be ionized; a dielectric tube in which the gas is ionized; a RF antenna working in the MHz regime which convey the ionization and heating power; coils or permanent magnets which surround the dielectric tube, and create a quasi-axial magnetic field in the range of hundreds of Gauss. The magnetic field: i) enhances the plasma confinement inside the source; ii) allows for an efficient power deposition into the plasma, by means of the Helicon waves dumping;[4] iii) creates a diverging magnetic field region at the dielectric tube exhaust, providing a magnetic nozzle effect. Therefore in a HPT we can distinguish between two main stages: an Helicon source which works as plasma production stage, and a magnetic nozzle which works as acceleration stage. In the magnetic nozzle the divergent magnetic field structure allows for the conversion of plasma thermal energy into axial kinetic energy. HPTs are characterized by the absence of electrodes and neutralizers, and a reduced interaction of plasma with walls (because of the magnetic field); therefore HPT are characterized by a long life (reduced erosion), and a good efficiency (reduced heat losses). HPTs are under study and development in some international research projects such as the American VASIMR,[5] where a high-power Helicon source is coupled to an ion cyclotron resonance heating section to increase the specific impulse; the Europeans HPH.COM[6] in which a low-power ($\leq$100 W) system has been developed, and SAPERE-STRONG[7] that aims at the realization of a high-power ($\geq$1 kW) propulsive system to be employed in a space tug. Other research centers which have developed HPTs prototypes are ANU,[8] MIT,[9] Tokio University,[10] and Madrid University.[11]

DOI: 10.13009/EUCASS2017-32

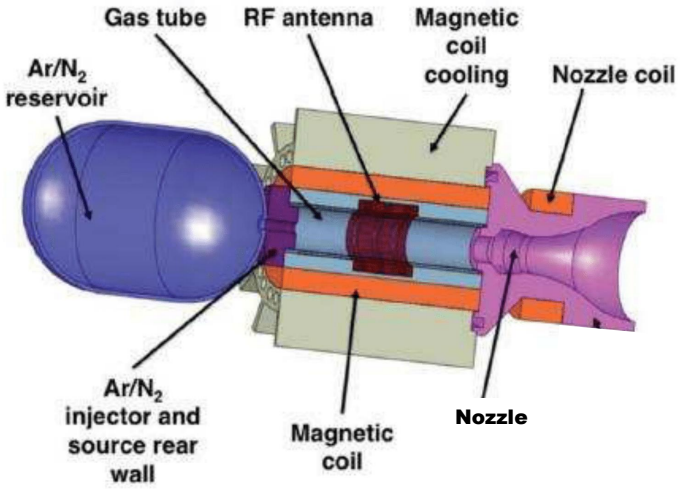

Figure 1: Helicon Plasma Thruster draft.

In order to optimize the propulsive figures of merit (e.g. specific impulse, thrust/mass ratio, and efficiency) of an HPT, we need to gain a deep physical insight into both the plasma generation and plasma acceleration mechanisms. In this work we will focus on the study of plasma source stage. Among different plasma sources Helicon sources are more efficient in conveying electromagnetic power into the plasma, therefore plasma density up to 10^{19} m^{-3} can be reached with a magnetic field below < 1000 G and a simple antenna geometry such as Single Loop antenna. Physics processes that occur in a Helicon plasma sources are: i) plasma generation, ii) wave-plasma coupling, and iii) plasma transport. Therefore we need theoretical and numerical models able to grasp these phenomena in order to design and possibly optimize an Helicon source devoted to space applications.

Simplified theoretical models of an Helicon plasma source for space application have been developed by Ahedo[12] and Lafleur;[13] these models are useful in the preliminary design but give not sufficient insight to perform source optimization. Standard numerical approaches rely on Electro-Magnetic (EM) solvers, which model the wave propagation and the power deposition therein, coupled to either kinetic[14] or Particle-In-Cell (PIC)[15–17] strategies to reproduce plasma response. However in high-power plasma sources, such as that required in the STRONG project, the plasma density can reach values higher than 10^{19} m^{-3}; such values can not be handled by a PIC code, while could result in a computational burden for a kinetic approach. Therefore, we will resort on a fluid strategy to reproduce the plasma transport in a high-power plasma source while keeping the computational cost at bay. Plasma fluid approaches have been widely employed for modeling of industrial plasma sources; in literature we can find fluid transport models of Capacitively Coupled Plasma sources (CCPs),[18] magnetically enhanced CCPs,[19] Inductively Coupled Plasma sources (ICPs),[20] and Helicon sources.[21,22]

We have developed a numerical tool devoted to the study and the optimization of Helicon plasma sources for space applications. The tool is realized by means of the integration of an EM solver and a fluid solver (section 2.1); the EM problem is solved with ADAMANT[24] (section 2.2), and the fluid transport model has been implemented in OpenFOAM[23] (section 2.3). We have developed three versions of our tool, namely 1D-axial, 1D-radial, and 2D-radial-axial. We have accomplished the simplest versions, namely 1D-axial and 1D-radial, in order to validate the EM-fluid coupling strategy, and thereafter the 2D-radial-axial version in order to model the source with a good degree of accuracy. In this paper we first present the benchmarking of the 2D-radial-axial version against a well-established solver[21] (section 3.1). Second, we have analyzed two source configurations (with and without magnetic field) with the three versions of the tool. For a fixed configuration we have compared the 2D-radial-axial solver against the simplified versions; moreover we have benchmarked our tool against a 0D model.[17] The aim of this analysis is to cross-validate the different versions of our tool among each other and against a 0D model, and, in turn, to understand when simplified models can give good predictions (section 3.2).

DOI: 10.13009/EUCASS2017-32

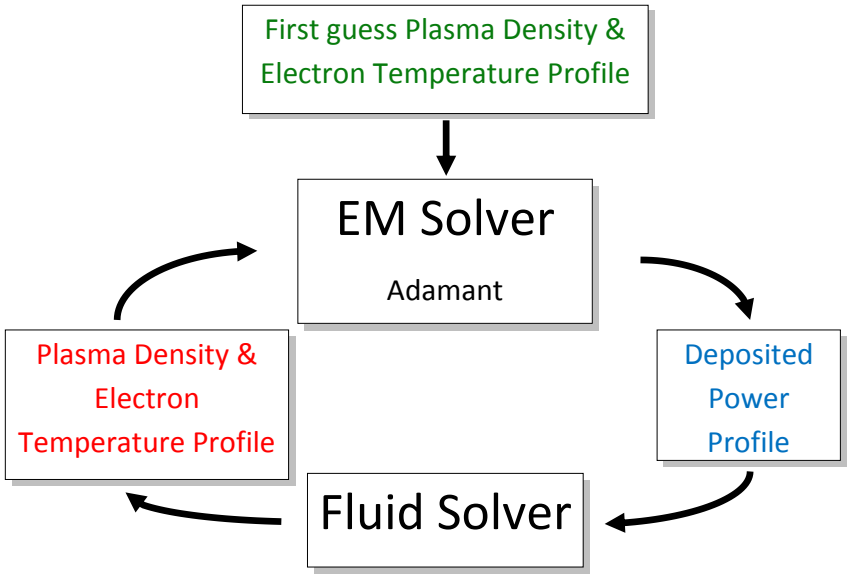

Figure 2: Sketch of the iterative loop.

2. Methodology

2.1 EM-Fluid Coupling

To model the coupling of the wave propagation and the plasma transport it is possible to study separately the electromagnetic and plasma dynamics phenomena. From a physical point of view, this approach is justified because the time scaling at which the two phenomena happen is different: the wave propagation is by far faster than the plasma diffusion. In the study of the plasma transport, the wave propagation can be retained as a source term through the power deposited by the antenna into the plasma; in the solution of wave propagation the plasma parameters (e.g., plasma density and electron temperature) can be considered as stationary. Wave propagation and plasma transport are solved by means of ADAMANT and OpenFOAM, respectively; both solvers are coupled by means of an iterative loop (see Figure 2). This loop is initialized with a first guess plasma parameters profile, usually uniform; the electromagnetic solver runs first and its output (the power deposited into the plasma) is the input for the fluid solver. Similarly, the output quantities of the fluid solver (plasma parameters profiles) are the input of the fluid solver. These two solvers will iterate until convergence criteria are satisfied; in this way we have obtained a consistent tool for source modeling.
In coupling ADAMANT with the fluid solver particular attention must be paid to avoid the introduction of numerical noise. In fact ADAMANT works only with 3D geometries while the input power profile of our fluid solver can be 1D-radial, 1D-axial or 2D-radial-axial. Therefore the local power deposition profile has to be sampled on the OpenFOAM structured mesh; in order to avoid the introduction of numerical noise during this operation a careful mesh analysis on both ADAMANT and OpenFOAM meshes has to be done.
We have developed three versions of the tool for the study of a cylindrical Helicon source: i) 1D-axial where we evaluate gradients of plasma parameters (e.g. plasma density and electron temperature) and power deposition profiles only along the axis of the source; ii) 1D-radial where the plasma is inhomogeneous only along the radius of the source; iii) 2D-radial-axial where we evaluate plasma inhomogeneities along both the radius and the axis of the source.

2.2 EM Model

The EM problem is solved with ADAMANT, a full-wave 3D numerical tool specifically conceived for the analysis and design of RF antennas which drives the discharge in Helicon plasma sources. ADAMANT solves for the surface electric current density on the antenna conductors and the volume polarization current within the plasma; the latter can be inhomogeneous and anisotropic whereas the antenna can have arbitrary shape. The plasma anisotropy is due to the presence of a magneto-static field, at the moment ADAMANT can treat only uniform magneto-static fields. The EM

DOI: 10.13009/EUCASS2017-32

problem is formulated in term of volume equations solved with the Method of Moments (MoM). ADAMANT allows for the accurate evaluation of the current distribution on the antenna and in the plasma, and in turn of the profile of the power deposition profile. ADAMANT relies on a 3D unstructured tetrahedral mesh, therefore we need to sample the power deposition profile given as ADAMANT's output on a 1D or 2D mesh if we are studying respectively a 1D or 2D problem.

2.3 Fluid Model

We have implemented the fluid model in OpenFOAM, an open source C++ library which solves differential problems with the MoM. OpenFOAM is designed for solving 3D problems and defines all meshes as such; however, 1D and 2D problems can be simulated by generating a mesh in 3D and applying special boundary conditions. In all the analyzed cases we have resorted on an hexahedral structured mesh.
In the fluid solver plasma is considered as a multi-fluid mixture composed of electrons, ions and neutrals. Electron density n_e and electron energy n_ε are solved through the drift-diffusion[25] approximated momentum and energy equations, ion n_i and neutral n_0 density are solved through the drift-diffusion form of the momentum equations (ion and neutral temperature are assumed equal to the initial gas temperature T_0), and an electrostatics model is employed to compute the plasma potential ϕ.

2.3.1 Governing Equations

The evolution of the k-th species (i.e. electrons, ions or neutrals) density is described by the continuity equation

$$\frac{\partial n_k}{\partial t} + \nabla \cdot \mathbf{\Gamma}_k = R_k \tag{1}$$

where n_k is the species density, $\mathbf{\Gamma}_k$ is the species flux vector and R_k is either a source or a sink of particles due to chemical reaction. In the drift diffusion approximation the equation of motion reduces to

$$\mathbf{\Gamma}_k = n_k \mathbf{v}_k = \pm \mu_k n_k \mathbf{E} - D_k \nabla n_k \tag{2}$$

where $\mathbf{v}_k$ is the species velocity, $\mathbf{E}$ is the electrostatic field , D_k the species diffusivity, and μ_k the species mobility. The sign of the mobility term is positive for ions, and negative for electrons; for neutrals the mobility contribution disappear because neutral particles are not affected by electric field.
The electron energy follows the energy equation

$$\frac{\partial n_\varepsilon}{\partial t} + \nabla \cdot \mathbf{\Gamma}_\varepsilon + \mathbf{E} \cdot \mathbf{\Gamma}_e = R_\varepsilon \tag{3}$$

where $\mathbf{\Gamma}_\varepsilon$ is the energy flux vector and R_ε is either a source or a sink of energy due to chemical reaction and external power sources. In the drift diffusion approximation the energy flux vector reads

$$\mathbf{\Gamma}_k = -\mu_\varepsilon n_\varepsilon \mathbf{E} - D_\varepsilon \nabla n_\varepsilon \tag{4}$$

where μ_ε is electron energy mobility and D_ε is the diffusion energy mobility.
The electrostatic potential is calculated via the Poissont equation

$$\nabla^2 \phi = -\frac{n_i - n_e}{\varepsilon_0} \tag{5}$$

where ε_0 is the vacuum permittivity.

2.3.2 Source Terms

The k-th species source term R_k which appears in the continuity equation depends on chemical reactions. We have considered an Ar discharge characterized by two reactions, namely elastic scattering and ionization

$$Ar + e \longrightarrow Ar + e \qquad \text{Elastic Scattering} \tag{6}$$

$$Ar + e \longrightarrow Ar^+ + 2e \qquad \text{Ionization} \tag{7}$$

therefore the only ionized species is single ionized Ar^+. We have assumed a Maxwellian Electron Energy Distribution Function (EEDF), therefore the reaction rate constants for elastic scattering k_{el} and for ionization k_{iz} can be calculated,

DOI: 10.13009/EUCASS2017-32

in function of the electron temperature T_e, following the empirical relations reported by Libermann and Lichtenberg.[26] The electron temperature is calculated as $T_e = (2n_\varepsilon)/(3n_e)$ being the EEDF Maxwellian. Therefore

$$R_e = R_i = -R_0 = k_{iz} n_e n_0 \tag{8}$$

The electron energy source terms R_ε depends on the power deposited into the source by RF antenna $\mathcal{E}_{Pow}$ and the chemical reactions power losses, namely the elastic loss $\mathcal{E}_{el} = -3m/MT_e R_{el}$ and the ionization loss $\mathcal{E}_{iz} = -\Delta_{iz} R_{iz}$; where m is the electron mass, M is the ion mass, and Δ_{iz} is the first ionization energy, for Ar $\Delta_{iz} = 15.80$ V. Therefore

$$R_\varepsilon = \mathcal{E}_{Pow} + \mathcal{E}_{el} + \mathcal{E}_{iz} \tag{9}$$

2.3.3 Transport Properties

In absence of any magneto-static field $\mathbf{B}_0$, electron mobility is calculated as

$$\mu_{e\ DC} = \frac{q}{m\ n_0\ (k_{el} + k_{iz})} \tag{10}$$

where q is the elementary charge. In presence of a magneto-static the mobility becomes a dyadic tensor

$$\mu_e^{-1} = \begin{pmatrix} \mu_{e\ DC}^{-1} & -B_{0z} & B_{0y} \\ B_{0z} & \mu_{e\ DC}^{-1} & -B_{0x} \\ -B_{0y} & B_{0x} & \mu_{e\ DC}^{-1} \end{pmatrix} \tag{11}$$

where B_{0j} is the $\mathbf{B}_0$ component along the j-th direction. Being EEDF Maxwellian we can apply the Einstain relations: $D_e = \mu_e T_e$, $\mu_\varepsilon = 5/3\mu_e$, $D_\varepsilon = \mu_\varepsilon T_e$.
The ion Ar^+ diffusion properties are calculated interpolating the experimental data reported by Chicheportiche.[27]
The neutral diffusivity D_0 is calculated considering only collisions among neutral Ar particles because we are dealing with weakly ionized gases.

2.3.4 Boundary Conditions

Ion and electron boundary conditions are given by the Bohm sheath criterion; the ion and electron fluxes perpendicular to the wall, and oriented outward the discharge, are

$$\Gamma_e = \Gamma_i = \sqrt{\frac{qT_e}{M}} n_i \tag{12}$$

The neutrals boundary condition is determined assuming that all the ions colliding the wall recombine in accordance with the wall reaction $Ar^+ \longrightarrow Ar$; therefore the neutral particles flux is equal to

$$\Gamma_0 = -\Gamma_i \tag{13}$$

The electron energy boundary condition is imposed in accordance with Mikellides[28]

$$\Gamma_\varepsilon = \left[\frac{T_e}{2} \left(1 + \ln \frac{M}{2\pi m} \right) + 2T_e \right] \Gamma_e \tag{14}$$

The grounded walls is the boundary condition for the Poissont equation

$$\phi = 0 \tag{15}$$

3. Benchmark

3.1 Comparison against a well-established solver

We have benchmarked our tool against a well-established solver, namely HEMP.[21] As reported in the Kinders' paper[21] we have studied a plasma cylinder of radius $R = 5$ cm, and length $L = 37.5$ cm. The system is powered by two ring coils with currents 180° out of phase (see Figure 1 of the reference paper[21]). The deposited power is Pw =1 kW, the initial neutral pressure is $p_n = 10$ mTorr. The best trade-off between accuracy and calculation time is approximately 9000 tets for the ADAMANT mesh, 100 structured elements in the radial direction and 200 structured elements in the axial direction for the OpenFOAM mesh. If we consider $B_0 = 10$ G a good agreement is found between the two models (compare Figure 5 of the reference paper[21] and Figure 3).

DOI: 10.13009/EUCASS2017-32

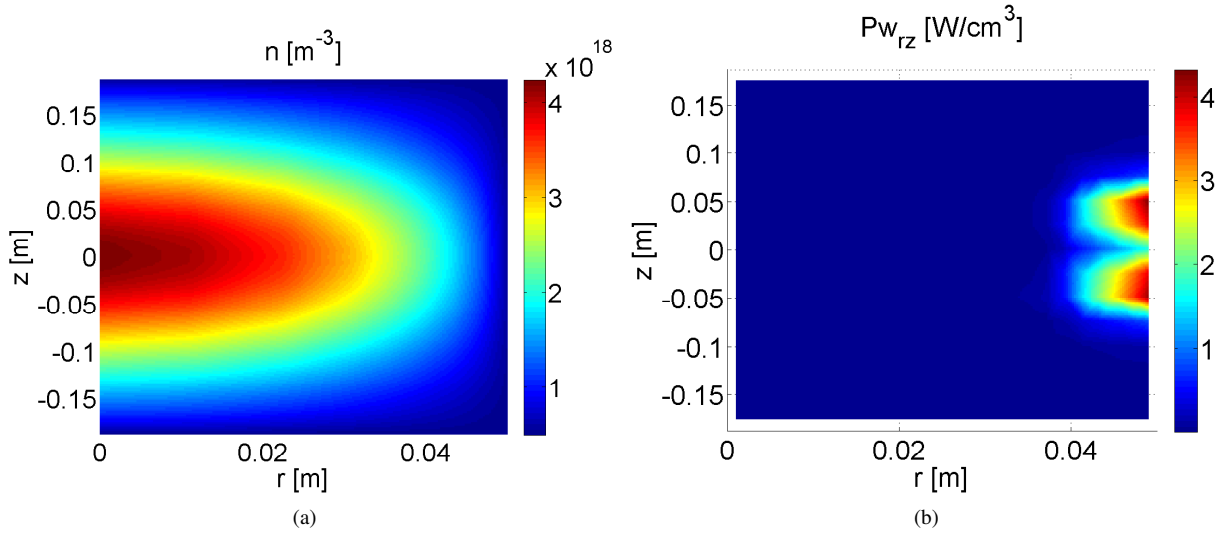

Figure 3: Low magnetic field $B_0 = 10$ G: a) electron density n, b) radial-axial deposited power profile Pw_{rz}.

3.2 Results

We have considered a plasma cylinder of radius $R = 2$ cm, height $L = 10$ cm, excited by a Single Loop antenna of radius $R_a = 3$ cm and width $w = 0.6$ cm (see Figure 4). The antenna if fed by a voltage gap $\Delta V = 500$ V, the initial neutral pressure is $p_n = 30$ mTorr. We have analyzed two cases: i) absence of magnetic field $B_0 = 0$ G, ii) presence of an axial magnetic field $B_0 = 500$ G. We have analyzed this configuration with a 1D-radial model (hereinafter referred to as *Radial Model*), a 1D-axial model (referred to as *Axial Model*), and a 2D-radial-axial model (referred to as *Radial Axial Model*); we have compared the results of our tool against a 0D global model (referred to as *Global Model*). The aim of this analysis is to identify the source configurations which can be studied with less computationally expensive models (e.g. *Global Model*) while retaining a good degree of accuracy.
The best trade-off between accuracy and calculation time is approximately

- *Axial Model*: 5500 tets for the ADAMANT mesh, 500 hexahedra for OpenFOAM mesh;
- *Radial Model*: 9000 tets for the ADAMANT mesh, 500 hexahedra for OpenFOAM mesh;
- *Radial Axial Model*: 9000 tets for the ADAMANT mesh, 100 hexahedra in the radial direction and 200 hexahedra in the axial direction for the OpenFOAM mesh.

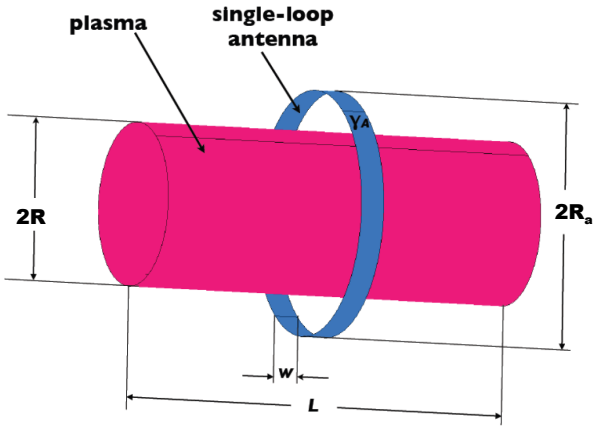

Figure 4: Helicon plasma source driven by a Single Loop antenna

DOI: 10.13009/EUCASS2017-32

3.2.1 *Radial Axial Model* results

Both in absence and in presence of magnetic field the equilibrium configurations present the same major features: i) plasma density n has a peak for $r = 0$ (near the cylinder axis) and for $z = 0$ (in the middle of the cylinder, below the antenna), as reported in Figure 5(a) and Figure 6(a); ii) the deposited power Pw_{rz} has a peak for $r = R$ (near the outer boundary) and $z = 0$, as reported in Figure 5(b) and Figure 6(b). The presence of the magnetic field increases the n peak value and reduces its width in the radial direction (compare Figure 5(a) and 6(a)).

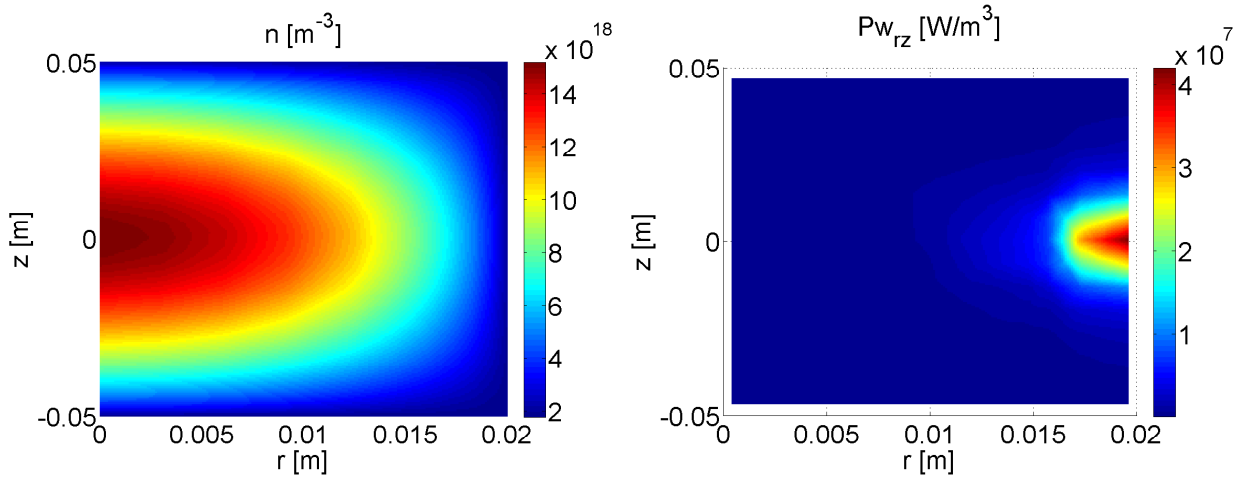

Figure 5: Equilibrium configuration calculated with *Radial Axial Model*. Absence of magnetic field, $B_0 = 0$ G. a) density profile, b) deposited power profile.

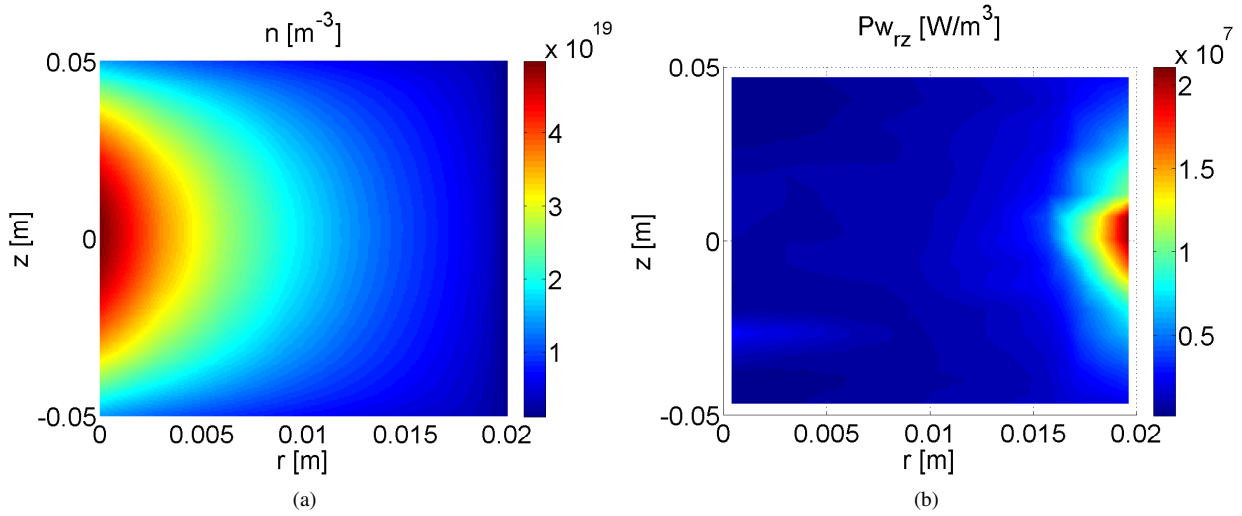

Figure 6: Equilibrium configuration calculated with *Radial Axial Model*. Presence of magnetic field, $B_0 = 500$ G. a) density profile, b) deposited power profile.

3.2.2 Comparison against the *Global Model*

If we integrate the results of *Radial Model*, *Axial Model*, *Radial Axial Model* we obtain the total power deposited into the source Pw and the average plasma density n_{avg}. In absence of magnetic field we have obtained the results reported in Table.1, in presence of magnetic field results are reported in Table.2. The *Axial Model* over-estimate both n_{avg} and Pw, this is due to the geometrical configuration considered: the plasma cylinder is prolate, therefore its lateral surface is larger than its top surface; *Global Model* and *Radial Axial Model* consider losses through the whole surface of the plasma cylinder, while *Radial Model* consider only losses from the side surface and *Axial Model* losses from the top

DOI: 10.13009/EUCASS2017-32

surface. If the top surface is a small part of the whole surface (like in this case) the *Axial Model* is highly inaccurate. The agreement between *Radial Model* and *Radial Axial Model* is good, while their agreement with *Global Model* is better in absence of magnetic field. This could happen because of the simplified diffusion model implemented in the *Global Model*.

	Global Model	***Radial Model***	***Axial Model***	***Radial Axial Model***
Pw [W]	480	375	592	383
n_{avg} [m^{-3}]	1.68×10^{19}	7.08×10^{18}	1.48×10^{20}	6.53×10^{18}

Table 1: Total power deposition Pw and average plasma density n_{avg} extimated with *Global Model*, *Radial Model*, *Axial Model*, *Radial Axial Model*. The considered axial magnetic field is $B_0 = 0$ G.

	Global Model	***Radial Model***	***Axial Model***	***Radial Axial Model***
Pw [W]	805	338	510	379
n_{avg} [m^{-3}]	3.05×10^{19}	6.39×10^{18}	1.30×10^{20}	1.09×10^{19}

Table 2: Total power deposition Pw and average plasma density n_{avg} extimated with *Global Model*, *Radial Model*, *Axial Model*, *Radial Axial Model*. The considered axial magnetic field is $B_0 = 500$ G.

3.2.3 Comparison against the *Axial Model*

As we expected from the comparison against the *Global Model*, we have a bad agreement between the *Axial Model* and the *Radial Axial Model* integrated in the radial direction (see Figure 7(a) and Figure 8(a)). This seems mainly due to the prolate shape of the plasma cylinder.

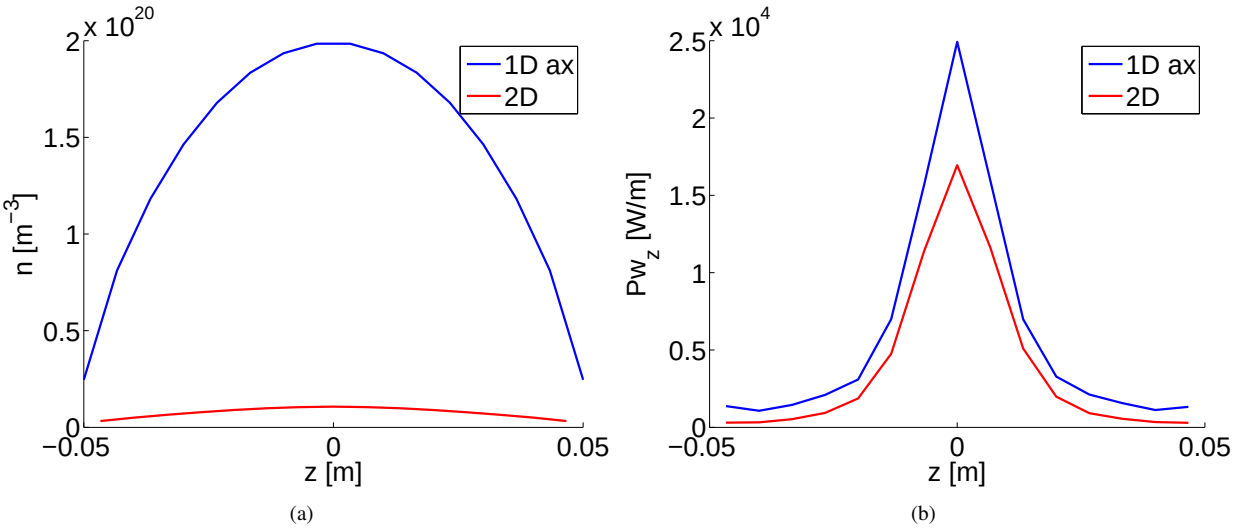

(a) (b)

Figure 7: Equilibrium configuration calculated with the *Axial Model* (1D ax), and *Radial Axial Model* (2D) integrated in the radial direction. Absence of magnetic field, $B_0 = 0$ G. a) axial density profile, b) axial power profile.

DOI: 10.13009/EUCASS2017-32

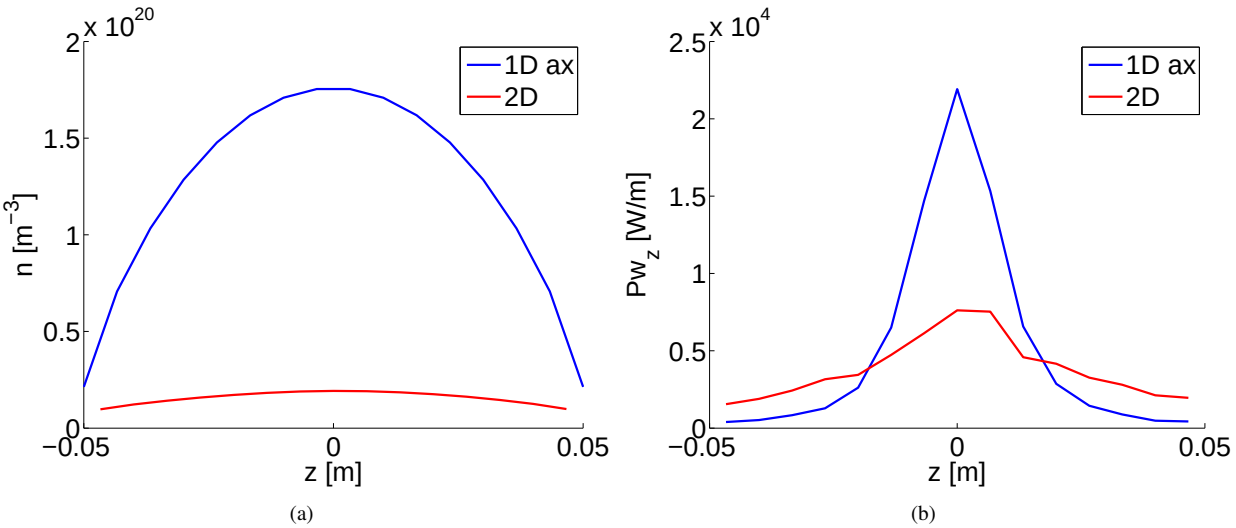

(a) (b)

Figure 8: Equilibrium configuration calculated with the *Axial Model* (1D ax), and *Radial Axial Model* (2D) integrated in the radial direction. Presence of magnetic field, B_0 = 500 G. a) axial density profile, b) axial power profile.

3.2.4 Comparison against the *Radial Model*

We have compared the results of the *Radial Model* and of the *Radial Axial Model* integrated in axial direction (in order to have an averaged information in the radial direction). A good agreement between the two models is found if $B_0 = 0$ G (see Figure 9). If B_0 = 500 G a good agreement between the power deposition profiles if found (see Figure 10(b)), however the coherence between the two models decreases in regard of the plasma density (see Figure 10(a)). This could be due to the different diffusion models applied: in the *Radial Model* diffusion coefficients are scalars while in the *Radial Axial Model* diffusion coefficients are dyadic tensors.

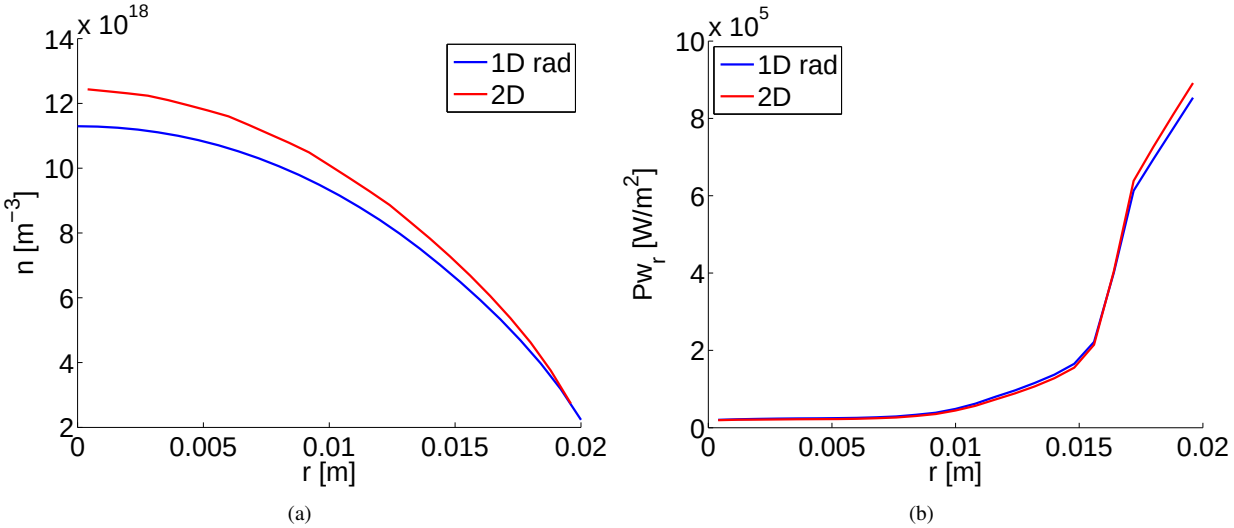

(a) (b)

Figure 9: Equilibrium configuration calculated with the *Radial Model* (1D rad), and the *Radial Axial Model* (2D) integrated in the axial direction. Absence of magnetic field, B_0 = 0 G. a) radial density profile, b) radial power profile.

DOI: 10.13009/EUCASS2017-32

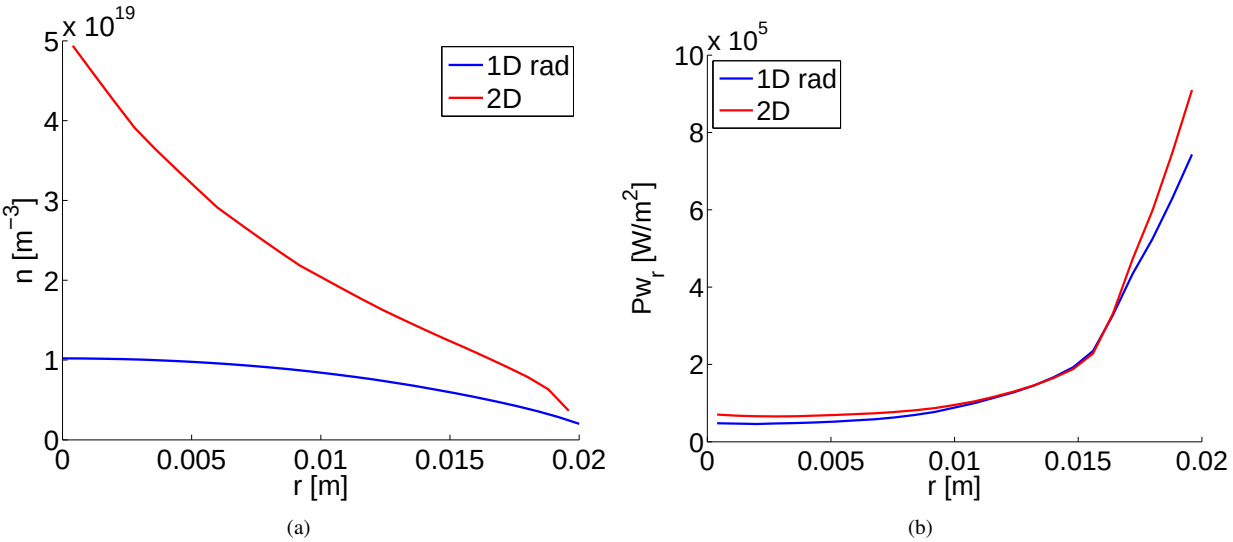

(a) (b)

Figure 10: Equilibrium configuration calculated with the *Radial Model* (1D rad), and the *Radial Axial Model* (2D) integrated in the axial direction. Presence of magnetic field, B_0 = 500 G. a) radial density profile, b) radial power profile.

4. Conclusions

We have realized a numerical tool specifically conceived to model a Helicon plasma source, coupling the EM problem (solved by ADAMANT) and the fluid problem (solved in OpenFOAM). We have successfully benchmarked our tool against a well-established tool. Depending on the level of accuracy required to the simulation, it is possible to choose among 1D-radial, 1D-axial, or 2D-radial-axial models of the source. All these models are able to grasp the main physical features of a Helicon source: power peak near the radial edge of the plasma cylinder, plasma density peak near the axis of the discharge. In particular in absence of any magnetic field the three models developed show a better agreement among themselves and with 0D global models. In a magnetized case it is advisable to employ the 2D model of the discharge because mobility and diffusivity are dyadic tensors. In future works we want to refine the fluid model, implementing a more accurate chemical model, and to evaluate the effects of solenoidal magnetic fields (removing the approximation of axial and uniform magnetic field).

References

[1] Edwards, C. H., et al. The T5 ion propulsion assembly for drag compensation on GOCE. *Second International GOCE User Workshop* GOCE, The Geoid and Oceanography. 2004.

[2] Wallace, N. "Testing of the Qinetiq T6 thruster in support of the ESA BepiColombo mercury mission for the ESA BepiColombo mission. *4th International Spacecraft Propulsion Conference*. Vol. 555. 2004.

[3] Chen, F. F., Helicon plasma sources, *High Density Plasma Sources*, 1995, pp. 1–75.

[4] Chen, F. F., and Arnush, D., Generalized theory of helicon waves I. Normal modes, *Phys. Plasmas*, Vol. 4, No. 9, 1997, pp. 3411–3421.

[5] Chang Diaz, F. R., The Vasimir, *Sci. Am.*, Vol. 283, No. 5, November 2000, pp. 90–97.

[6] Pavarin, D., et al., Helicon Plasma Hydrazine Combined Micro Project Overview and Development Status, *Proceedings of the Space Propulsion Conference*, San Sebastian, Spain, 2010.

[7] Official CTNA web site, http://www.ctna.it/projects/

[8] Boswell, R. W., et al., The helicon double layer thruster, *28th International Electric Propulsion Conference*, IEPC. 2003.

DOI: 10.13009/EUCASS2017-32

[9] Batishchev, O. V., Mini-helicon plasma thruster, *IEEE Transactions on Plasma Science*, vol.37, issue 8, pp.1563-1571, 2009.

[10] Shinohara, S., et al., Development of electrodeless plasma thrusters with high-density helicon plasma sources, *IEEE Transactions on Plasma Science* 42.5: 1245-1254, 2014.

[11] Merino, M., et al., Design and development of a 1 kW-class helicon antenna thruster, *34th International Electric Propulsion Conference*, IEPC-2015-297 (Electric Rocket Propulsion Society, Fairview Park, OH, 2015). 2015.

[12] Ahedo, E., Navarro-Cavalle, J., Helicon thruster plasma modeling: Two-dimensional fluid-dynamics and propulsive performances. *Physics of Plasmas*, 20.4: 043512, 2013.

[13] Lafleur, T., Helicon plasma thruster discharge model. *Physics of Plasmas* 21.4 (2014): 043507.

[14] Batishchev, O., and Molvig, K., Kinetic model of a helicon plasma source for VASIMR. *39th Aerospace Sciences Meeting and Exhibit*. 2001.

[15] Pavarin, D., et al., Development of Plasma Codes for the Design of Mini-Helicon Thrusters. (2011).

[16] Pavarin, D., et al., Design of 50 W helicon plasma thruster. *31st Int. Electric Propulsion Conf.*, Ann Arbor, MI. 2009.

[17] Manente, M., et al., Numerical simulation of the Helicon double layer thruster concept. *43rd AIAA/ASME/SAE/ASEE Joint Propulsion Conference & Exhibit*. 2007.

[18] Shahid, R., Kenney, J., Collins, K., Three-dimensional model of magnetized capacitively coupled plasmas. *Journal of Applied Physics* 105.10 (2009): 103301.

[19] Kushner, M. J., Modeling of magnetically enhanced capacitively coupled plasma sources: Ar discharges. *Journal of applied physics* 94.3 (2003): 1436-1447.

[20] Bukowski, J. D., Graves, D. B. , Vitello, P., Two–dimensional fluid model of an inductively coupled plasma with comparison to experimental spatial profiles. *Journal of Applied Physics* 80.5 (1996): 2614-2623.

[21] Kinder, R. L., Kushner, M. J., Wave propagation and power deposition in magnetically enhanced inductively coupled and helicon plasma sources. *Journal of Vacuum Science & Technology* A: Vacuum, Surfaces, and Films 19.1 (2001): 76-86.

[22] Bose, D., Govindan, T. R., Meyyappan, M., Modeling of a helicon plasma source. *IEEE transactions on plasma science* 31.4 (2003): 464-470.

[23] Jasak, H., Jemcov, A., Tukovic, Z., OpenFOAM: A C++ library for complex physics simulations. *International workshop on coupled methods in numerical dynamics*. Vol. 1000. IUC Dubrovnik, Croatia, 2007.

[24] Melazzi, D., Lancellotti, V., ADAMANT: A surface and volume integral-equation solver for the analysis and design of Helicon plasma sources. *Computer Physics Communications* 185.7 (2014): 1914-1925.

[25] Fiala, A., Pitchford, L., Boeuf, J. P., Two-dimensional,hybrid model of low-pressure glow discharges. *Phys Rev* E1994;49:5607–24. http://dx.doi.org/10.1103/PhysRevE.49.5607.

[26] Lieberman, M. A., Lichtenberg, A. J., Principles of plasma discharges and materials processing. John Wiley & Sons, 2005, chap.3, pp 81.

[27] Chicheportiche, A., et al., Ab initio transport coefficients of Ar+ ions in Ar for cold plasma jet modeling. *Physical Review* E 89.6 (2014): 063102.

[28] Mikellides, I. G., et al., Hollow cathode theory and experiment. II. A two-dimensional theoretical model of the emitter region. *Journal of Applied Physics* 98.11 (2005): 113303.